ACS Photonics

Article

pubs.acs.org/journal/apchd5

Exploiting Native Al_2O_3 for Multispectral Aluminum Plasmonics

Sencer Ayas,* Ahmet Emin Topal, Andi Cupallari, Hasan Güner, Gokhan Bakan, and Aykutlu Dana*

UNAM Institute of Materials Science and Nanotechnology, Bilkent University, Bilkent, 06800 Ankara, Turkey

Supporting Information

ABSTRACT: Aluminum, despite its abundance and low cost, is usually avoided for plasmonic applications due to losses in visible/infrared regimes and its interband absorption at 800 nm. Yet, it is compatible with silicon CMOS processes, making it a promising alternative for integrated plasmonic applications. It is also well known that a thin layer of native Al_2O_3 is formed on aluminum when exposed to air, which must be taken into account properly while designing plasmonic structures. Here, for the first time we report exploitation of the native Al_2O_3 layer for fabrication of periodic metal−insulator−metal (MIM) plasmonic structures that exhibit resonances spanning a wide spectral range, from the near-ultraviolet to mid-infrared region of the spectrum. Through fabrication of silver nanoislands on aluminum surfaces and MIM plasmonic surfaces with a thin native Al_2O_3 layer, hierarchical plasmonic structures are formed and used in surface-enhanced infrared spectroscopy (SEIRA) and surface-enhanced Raman spectrocopy (SERS) for detection of self-assembled monolayers of dodecanethiol.

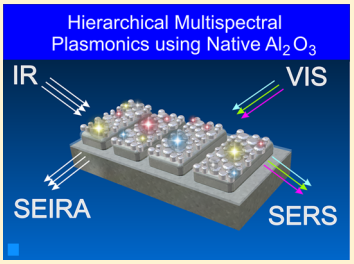

KEYWORDS: *aluminum plasmonics, metal−insulator−metal cavities, surface-enhanced Raman spectroscopy, surface-enhanced infrared spectroscopy, nanoparticles, hierarchical structures*

Recent advancement in plasmonics enabled the development of better performing plasmonic materials for the ultraviolet (UV)[1−5] and infrared (IR)[6−13] portion of the light spectrum. Typically gold (Au) and silver (Ag) are the most common materials used to fabricate nanostructures to study novel plasmon-enhanced materials and enable optical phenomena such as negative refraction,[14,15] transformation optics,[16] surface plasmon sensors,[17,18] surface-enhanced Raman spectroscopy (SERS),[19,20] surface-enhanced infrared absorption spectroscopy (SEIRA),[21,22] and plasmon-enhanced solar cells and detectors.[23,24] Au has an internal band transition around 500 nm, which limits utilization of gold toward the UV portion of the visible spectrum.[25] Due to its chemically inert properties, stability, and tailorable binding to biomolecules, Au is widely used for surface plasmon resonance sensor applications working at visible wavelengths closer to the NIR regime. Ag is considered the optimal material for plasmonic applications in the visible spectrum due to its low loss compared to other metals.[25] However, Ag suffers from atmospheric sulfur contamination and oxidation.[26] Aluminum arises as a promising material for UV[27,28] and deep UV plasmonic applications[3,4,29−31] owing to its high plasma frequency. Al has high losses from the visible to IR range as well as an interband absorption around 800 nm, which makes it less favorable as a NIR plasmonic material.[1,25,32] Still, localized plasmon resonances in Al have been demonstrated in several geometries, including nanoparticles,[27,30,33] triangles,[3,28,34] discs,[4,35,36] rods, and nanoantennas.[31,37,38] The relative abundance of Al can be advantageous for the design of plasmonic absorbers in solar energy conversion or for inexpensive, disposable SERS and fluorescence-enhancing substrates. Due to complementary metal oxide semiconductor (CMOS) compatibility, Al plasmonic nanostructures would be optimal for silicon-integrated optoelectronic applications, such as integrated biomolecular sensing,[39,40] on-chip plasmonic nanoantennas, waveguides, and interconnects.[14,41−44] Furthermore, the surface oxide of Al self-terminates at a thickness of 3−5 nm, forming a durable protective layer and preserving the metal, making this material a convenient choice for plasmonic applications that require durability.[45,46] Here, we demonstrate exploitation of the native oxide (NO) layer to form metal−insulator−metal (MIM) structures with resonances spanning a wide spectral range by enabling an extreme mode confinement limit where multiple modes can be excited on the same structure due to an ultrathin native oxide spacer layer. Nanoparticle-based MIM structures are demonstrated over large areas using a thin dewetting Ag top layer near the percolation threshold on naturally oxidized aluminum. The optical properties of such MIM structures are tuned by simply allowing a thicker native oxide layer to form by longer exposure to ambient conditions. The native oxide also allows simple fabrication of hierarchical plasmonic surfaces that exhibit simultaneous resonances in the visible and infrared regimes. Such hierarchical multispectral MIM structures feature simultaneously SERS and SEIRA.

RESULTS AND DISCUSSION

Periodic MIM structures on aluminum bottom layers are studied where the insulator is the native oxide layer, which is naturally formed during the fabrication process, which eliminates the need for depositing an insulator layer. Typically, the fabrication process of native oxide based MIM (NO-MIM) structures requires multiple metal deposition processes (see

Received: September 8, 2014
Published: November 18, 2014

   dx.doi.org/10.1021/ph500330x | ACS Photonics 2014, 1, 1313−1321

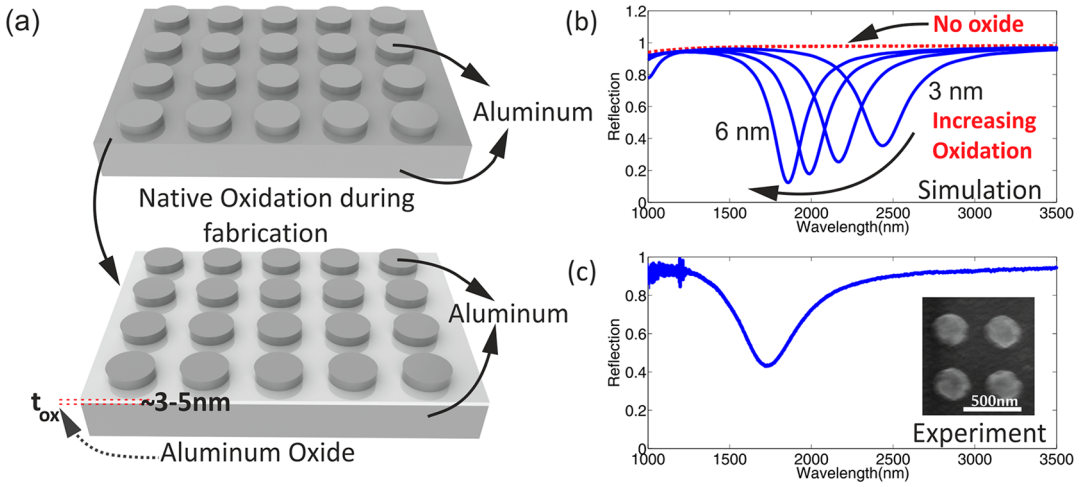

Figure 1. Verification of NO-MIM structures through observations of resonances in the NIR. (a) Schematic of formation of NO-MIM surfaces during the fabrication process (top patterned layer height is 50 nm). (b) Simulated reflectance spectrum of NO-MIM structures for various Al_2O_3 thicknesses. While no plasmonic resonance is observed in the absence of native oxide, plasmonic resonances in the NIR are observed due to the native oxide layer. Resonances blue-shift with increasing oxide thickness. (c) Experimental reflection spectra of the fabricated nanodisc NO-MIM structure. Diameter and period of the discs are 250 and 400 nm, respectively. (Inset) SEM image of the nanodisc array.

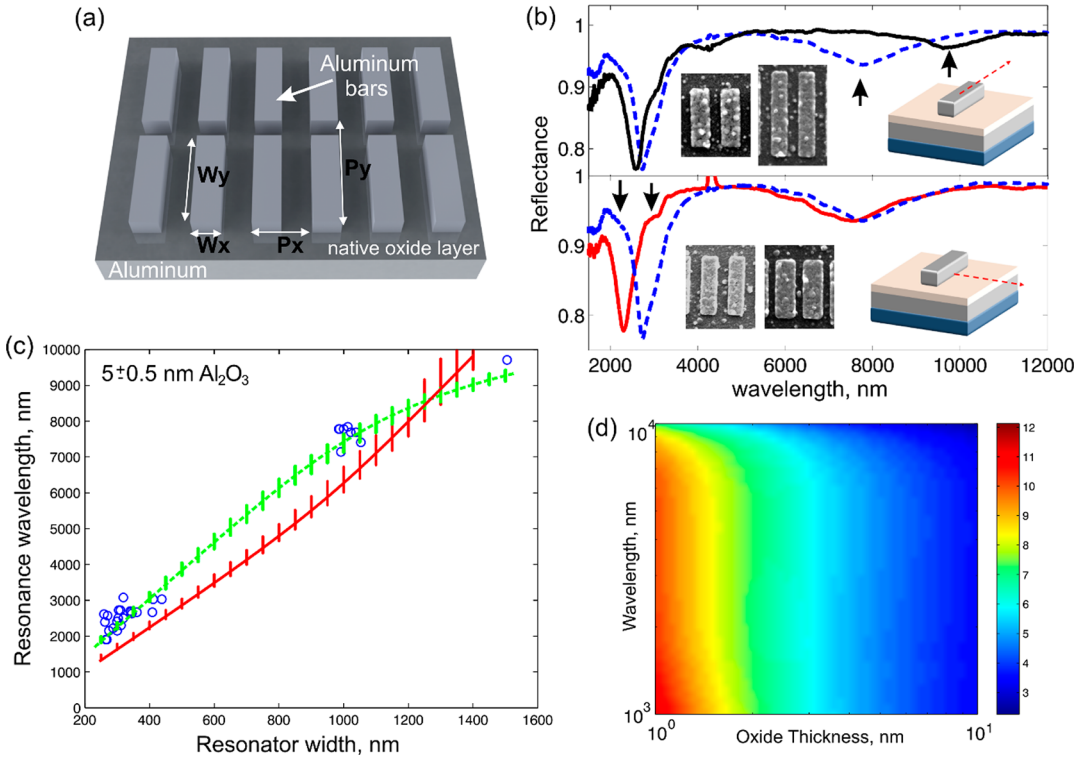

Figure 2. Resonance tuning in the NIR and MIR range using anisotropic Al bar arrays. (a) Schematic of asymmetric NO-MIM structures with nonidentical periods and widths along the x and y directions to excite multiple modes in the IR (top patterned layer height is 50 nm). (b) Typical reflection spectra showing multiple resonances in the NIR and MIR range due to the asymmetry of the structures with P_x = 500 nm, P_y = 2000 nm, and W_x = 310 nm for W_y = 1000 nm (black curve), 1500 nm (blue curve) (top) and W_x = 250 nm (red curve), 310 nm (blue curve) for W_y = 1000 nm (bottom). (Inset) SEM images of corresponding structures. Red dashed lines indicate the axis on which the structures' width is modified. (c) Experimentally observed resonance wavelengths as functions of the Al bar width along either the short or long axis (blue dots). Calculated resonances by treating the NO-MIM structures as Fabry–Perot (FP) resonators consisting of truncated waveguides (green and red curves). A better fit of the FP resonator model to the experiments can be achieved if the dielectric function of Al_2O_3 is assumed to be wavelength dependent (green curve), as opposed to a constant (red curve, n = 1.6). Vertical lines on the curves are error bars corresponding to 0.5 nm uncertainty in the oxide thickness. (d) Effective refractive index of the waveguide forming the FP resonator as a function of Al_2O_3 thickness, using the wavelength-dependent dielectric function.

Figure S1). After depositing the first Al layer, the vacuum is broken for poly(methyl methacrylate) (PMMA) coating and e-beam lithography, which is accompanied by formation of a thin layer of Al_2O_3 on the surface of Al. The first set of plasmonic structures are formed through fabrication of nanodisc arrays on a silicon substrate coated with a thick layer of aluminum to

dx.doi.org/10.1021/ph500330x | ACS Photonics 2014, 1, 1313−1321

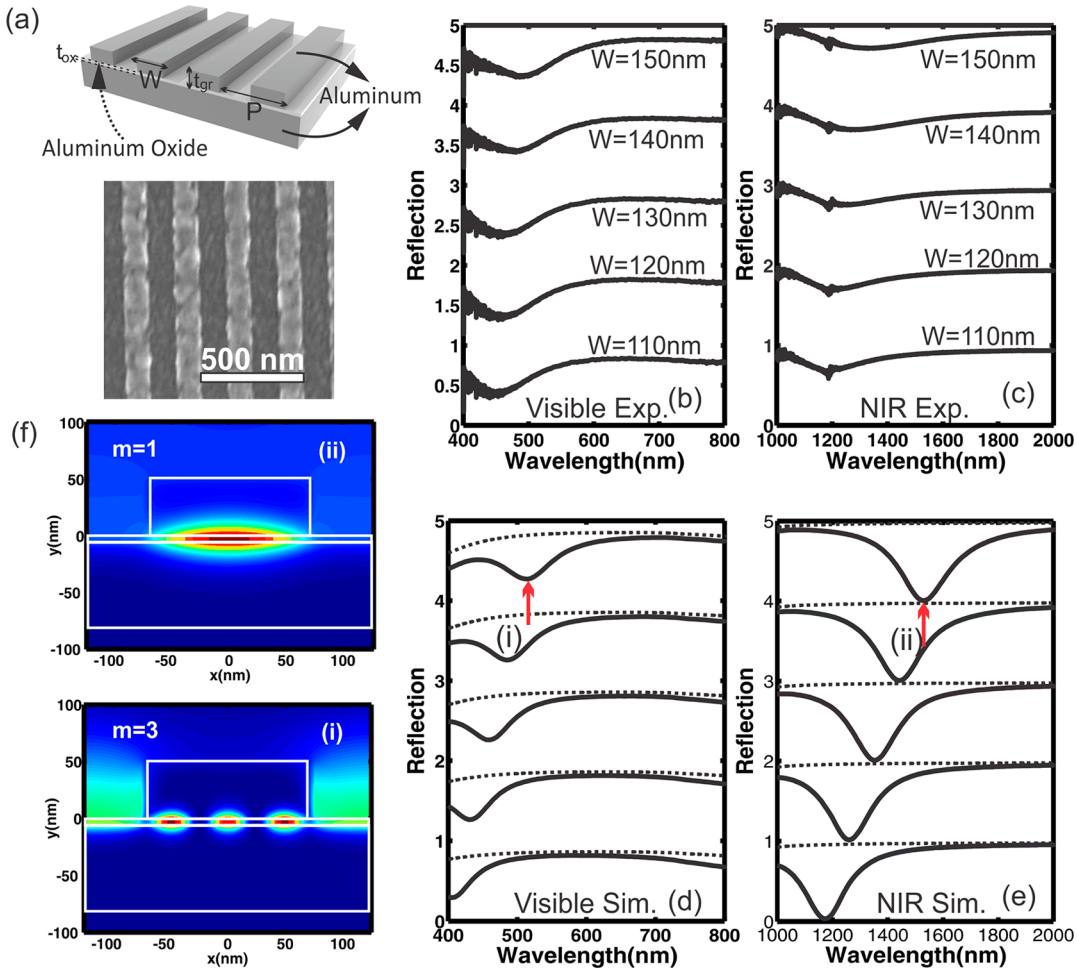

Figure 3. Simultaneous resonances in the visible and NIR regime using 1D NO-MIM. (a) Schematic of 1D NO-MIM structures. t_{gr} = 50 nm and P = 250 nm. Experimental results showing tuning of resonance wavelengths as W changes between 110 and 150 nm, (b) in the visible, and (c) in the NIR regime. (d, e) Simulation results for the experimented structures, which are in good agreement with the experimental results. Each spectrum curve is shifted by 1 along the y-axis for clarity. (f) First-order (m = 1) and third-order (m = 3) mode profiles corresponding to NIR (ii) and visible (i) resonances as indicated with arrows in (d) and (e). The even mode (m = 2) is not observed for normal incidence. In the simulations a native oxide layer thickness of 5 nm is assumed.

demonstrate NIR resonance due to the presence of native oxide. Figure 1a illustrates the formation of NO-MIM plasmonic surfaces with a top nanodisc array. The fabricated NO-MIM structures show a resonance at the NIR regime (Figure 1c) as characterized by a Fourier transform infrared reflection (FTIR) microscope system equipped with a 15× Cassegrain objective. A knife edge aperture is used to limit the measurement area to regions containing lithographically defined structures (100 μm × 100 μm). FDTD calculations show that a resonance emerges with the presence of a thin Al_2O_3 layer and blue-shifts with increasing oxide thickness (Figure 1b). Evolution of the native oxide thickness is monitored by X-ray photoelectron spectroscopy (XPS), as shown in Figure S2. Uniformity of the oxide thickness is verified by XPS measurements at various spots on a continuous Al film. The thickness of the native oxide layer is also characterized by spectroscopic ellipsometer measurements. However, it is not possible to determine the exact value of the native aluminum oxide thickness due to the surface roughness of aluminum. Neglecting the surface roughness of Al, which has a 1.5 nm RMS value, the thickness of the native oxide layer is found to be 5.2 nm after 24 h of exposure to air (20 °C, 35% relative humidity).

In order to demonstrate the versatility and tunability of NO-MIM structures, anisotropic structures that support resonances in the NIR and MIR regimes are investigated with long and short axis periods of 2 μm by 500 nm, respectively. A schematic of these structures is shown in Figure 2a. SEM images of the fabricated structures are shown in Figures 2b and S3. Tunability of reflection spectra by increasing either the long or short axis width is shown in Figure 2b. The reflection depths get weaker at these wavelengths due to weaker coupling of long wavelengths to the thin native oxide layer (see Figure S4 for the simulations). In an MIM cavity the effective propagation constant and effective refractive index depend on the thickness of the dielectric film. The plasmonic resonances are strongly dependent on the period and the width of the surfaces. Within a first-order approximation, the MIM mode of a patterned surface can be modeled as a standing wave that reflects back and forth from the edges of the top patterned layer, where individual resonators are assumed to be noninteracting. For closely spaced MIM resonators, coupling becomes important. The period of MIM structures affects the coupling of these individual nanocavities, and typically for a constant MIM width, the interaction increases for smaller periods due to stronger intercavity coupling. Otherwise, the period of an array of MIM

dx.doi.org/10.1021/ph500330x | ACS Photonics 2014, 1, 1313−1321

resonators is assumed to be nondominant in determining the individual resonator response. In order to find the resonance wavelengths, one has to solve the characteristic equation given by

$$W_{S,L}\frac{2\pi}{\lambda}n_{eff} = \pi - \phi_{S,L} \quad (1)$$

where $W_{S,L}$ are the widths along the short and long axes, n_{eff} is the effective refractive index of the propagating mode and $\varphi_{S,L}$ is the phase term due to the reflection from the terminations. The effective refractive index, n_{eff}, is calculated by solving the Maxwell equations analytically for a continuous MIM waveguide as shown in Figure 2d. Figure 2c shows the calculated resonance frequencies of NO-MIM modes with experimentally measured resonance frequencies for varying widths along either the short or long axes. An Al_2O_3 thickness of 5 ± 0.5 nm is deduced from the model, which agrees well with the ellipsometer measurements. It is observed that a dispersive dielectric function explains the observed resonance frequencies better than a constant dielectric function for Al_2O_3. Moreover, the cavity size of 1000 nm × 310 nm asymmetric resonators is about $\lambda^3/500\,000$ assuming a 5 nm thick native oxide layer.

A simple MIM structure with 1D Al bar array offers tunable, simultaneous resonances in both the visible and NIR regime due to accommodation of the first and higher order modes when the period and width of 1D structures are chosen properly (P = 250 nm). Only odd-order modes are excited for normal illumination, due to symmetry. Even-order modes can be excited at oblique angles due to the broken symmetry condition. Schematic and an SEM image of the fabricated 1D NO-MIM structures are shown in Figure 3a. Figure 3b shows the measured reflection spectra for the visible regime with increasing 1D structure width. The reflection spectra are measured with fiber coupled white light, polarized along the grating axis, using reflection from an aluminum mirror as the reference. Resonance wavelength red-shifts with increasing width (Figure 3b). NIR reflectance spectra of the same structures are measured with the FTIR microscope using an unpolarized NIR light source (Figure 3c). The resonance wavelength starts from 1200 nm and shifts to 1400 nm with increasing width. Measured visible and NIR reflectance spectra agree well with the simulations shown in Figure 3c,d. Simulations performed with neglecting NO show no distinct resonances, which also indicates that the resonances are due to the presence of a native oxide layer. Although almost zero reflection is observed in the simulations, the reflection depths for NIR measurements are smaller compared to the simulated values due to the use of unpolarized light. Surface roughness is neglected in the simulations, which might account for some of the discrepancies such as resonance wavelength mismatch between experiments and simulations. Magnetic field distributions are simulated as shown in Figure 3f to further understand the origin of the observed visible and NIR resonances. Magnetic field is confined to the oxide layer for both resonances. For the NIR resonance, the first-order or fundamental mode is excited. For the visible, third-order resonance is excited where there are three magnetic field peaks in the oxide layer ($\lambda_1 \cong 3\lambda_3$).

The studies presented here so far include a lithography step to pattern the top layer, which always yields a native oxide layer. To study the existence of a native oxide layer, NO-MIM structures based on self-forming Ag nanoparticles on the Al bottom layer are fabricated with and without exposing the Al layer to air by breaking the vacuum. Such an approach also offers larger area plasmonic surfaces compared to top-down fabrication techniques such as e-beam lithography and focused ion beam milling. For this study, Ag nanoparticles with an average size of 25 nm are obtained by evaporating a 3 nm Ag film (see Figure S5). Exposing Al surfaces to air for a longer duration, hence forming a thicker oxide, causes a blue-shift in the reflection spectrum (Figure 4a). Sequential deposition of

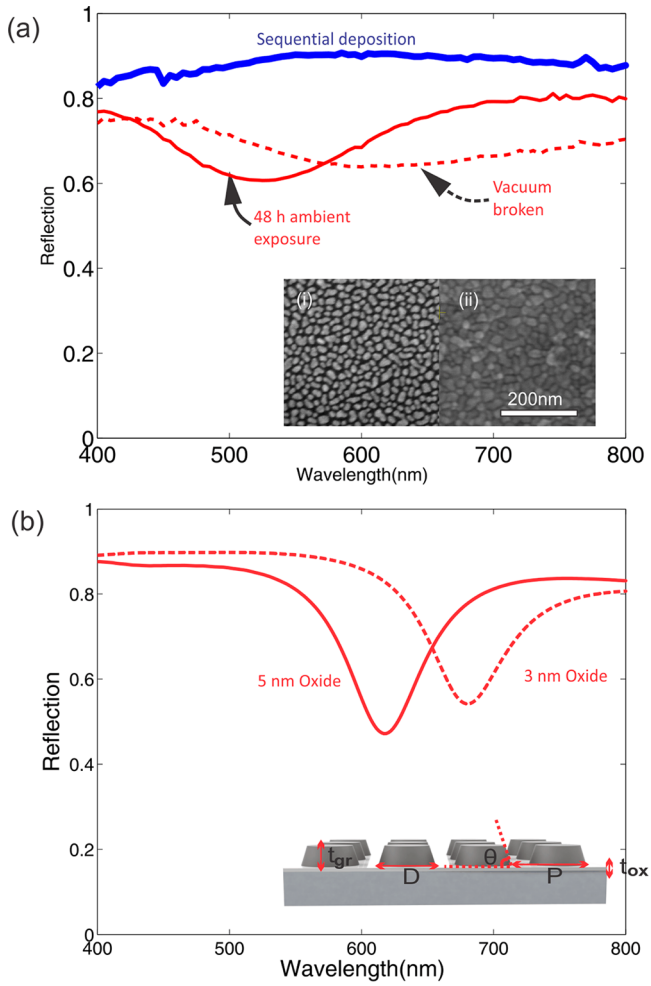

Figure 4. Nanoparticle-based large-area NO-MIM structures. (a) Reflection spectra for Ag nanoparticle based NO-MIM structures. The resonance blue-shifts if the time period between two deposition processes increases (dashed and solid red lines). No resonance is observed if the deposition of Al and Ag is done without breaking the vacuum (blue solid line). (Inset) SEM images of 3 nm Ag on Si(I) and Al(II). (c) Simulation results and simulated structure (inset) for t_{ox} = 3 and 5 nm. Simulated structure is a periodic array of truncated cones with D = 35 nm, P = 40 nm, t_{gr} = 20 nm, and θ = 75°.

Ag on Al films without breaking the vacuum does not show a resonance due to lack of an oxide layer. The effect of a native oxide layer on Ag nanoparticle based MIM structures is simulated by modeling the nanoparticle film as an array of truncated cones, as seen in Figure 4b. Increasing exposure time is captured through increasing the NO thickness in the simulations, which shows a blue-shift.

The studied plasmonic structures are used by sensing organic materials under Raman and infrared absorption spectroscopy, which gives information about the molecular structures and

dx.doi.org/10.1021/ph500330x | ACS Photonics 2014, 1, 1313−1321

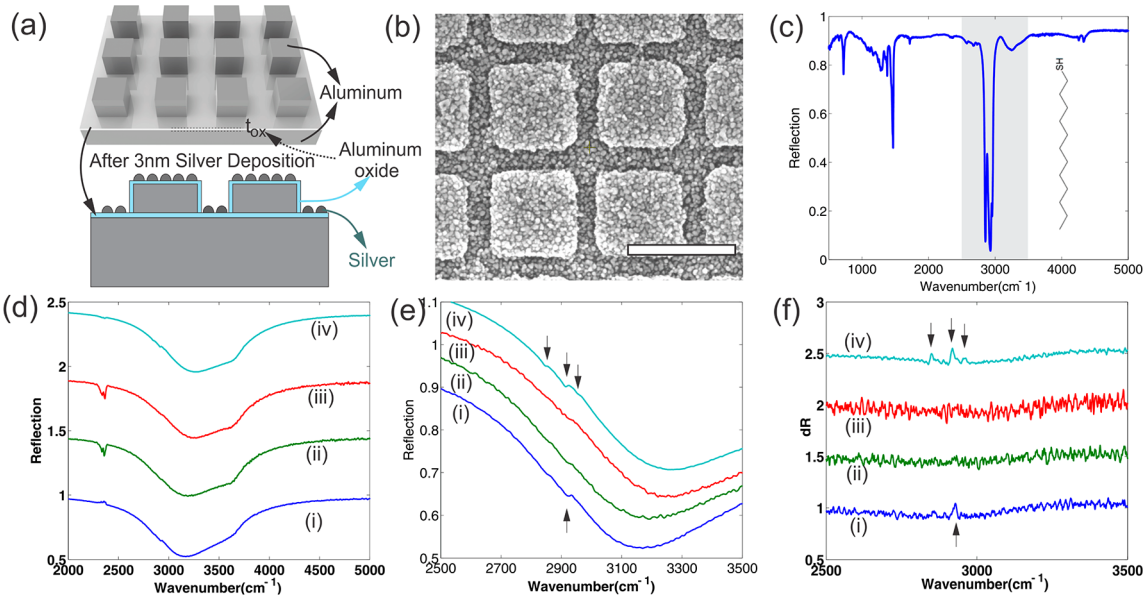

Figure 5. SEIRA detection of molecular monolayers on hierarchical NO-MIM structures. (a) Schematic of hierarchical NO-MIM structures before and after nanoparticle deposition with top patterned layer height of 50 nm. Periods and widths along the x and y directions are the same, $P_x = P_y =$ 500 nm and $W_x = W_y =$ 350 nm. (b) SEM image of NO-MIM structures after 3 nm Ag deposition (scale bar: 500 nm). (c) FTIR reflection spectrum of a thick DDT solution on a bare Al film. Region of interest is highlighted in gray. (Inset) Molecular sketch of DDT molecule. (d) FTIR reflection spectra of NO-MIM structures (i) just after fabrication of all Al NO-MIM structures, (ii) after plasma cleaning of PMMA residues, (iii) after the formation of hierarchical NO-MIM structures by 3 nm Ag deposition, and (iv) after DDT molecular monolayer formation on hierarchical NO-MIM structures. (e) FTIR reflectance between 2500 and 3500 cm^{-1} and its derivative (f) for better visualization of stretching of monolayer DDT molecules. Arrows mark the DDT and PMMA signatures in (e). Molecular signatures (2930 and 2955 cm^{-1}) of PMMA are observable before oxygen plasma cleaning. No distinctive bands are observed after oxygen plasma (ii) and Ag deposition (iii).

vibration spectra of molecules. The symmetry requirements in these two phenomena are different, and they give complementary information about a molecule. Typically, a high concentration of molecules is required in these techniques. On the other hand, SERS and SEIRA can magnify the signal levels up to 10^8-fold, where resonant light structures are used to enhance field intensities, enabling observation of the molecular vibrational signatures from a few molecules. By taking advantage of multispectral characteristics of NO-MIM surfaces we demonstrate SERS and SEIRA on the same structures. In the experiments dodecanethiol (DDT) is used as the probe molecule. DDT cannot form a monolayer on aluminum. However, DDT molecular formation on Ag has been long studied.[47] Therefore, we first tried to demonstrate SEIRA on NO-MIM structures with a Ag top layer ($Ag/Al_2O_3/Al$). The resonance frequency of the structures is around 3500 cm^{-1}, which is close to the C−H stretching of both DDT and PMMA (2930 and 2955 cm^{-1}) (Figure S6). However, during fabrication, resist residues, i.e., PMMA for e-beam lithography, are left on or under the patterned metals, resulting in vibrational signatures coinciding with those of DDT. Despite the presence of PMMA residues, the molecular signature of DDT after monolayer formation can be observed, as shown in Figure S6. The number of molecules contributing to the SEIRA signal is estimated to be 4.6 femtomoles on such periodic structures. Less than 1 attomole sensitivity can be achieved by taking measurements from a single NO-MIM resonator if a light source with very high signal to noise ratio is used such as a synchrotron light source.[48] The SEIRA enhancement factor is calculated as 2200 for these structures using a bare Ag film as the reference (Figure S7). In order to eliminate PMMA signatures from residues, the NO-MIM structures are treated in oxygen plasma. Since, oxygen plasma deteriorates the top silver layer, a different type of resonator structure with multiple hierarchical MIM cavities is developed. Figure 5a illustrates the hierarchical NO-MIM (metal−insulator−metal−insulator−metal, MIMIM) structures developed for SEIRA measurements to eliminate the PMMA residues with oxygen plasma. Oxygen plasma does not harm Al, but increasees oxide thickness on Al slightly. The fabrication steps of such structures are shown in Figure S8. First, an all-aluminum NO-MIM structure is fabricated by e-beam lithography with 500 nm period and 350 nm width that exhibits resonance in the IR (around 3500 cm^{-1}). Then the structures are cleaned in oxygen plasma, for PMMA residue removal. By evaporating 3 nm of Ag on cleaned $Al/Al_2O_3/Al$ resonators, final MIMIM structures are obtained (see Figure S8). Simulations show that depositing Ag nanoparticles on the Al NO-MIM structures changes these structures' reflection spectra significantly in the visible regime, whereas it only causes a slight blue-shift in the IR regime (Figure S9). Figure 5b shows the SEM image of the fabricated structure. Ag nanoparticles are formed both on and between the rectangular Al patterns. We first measured the FTIR reflection spectra of a DDT solution on a bare Al surface to determine the molecular bands of DDT close to resonance of the fabricated structures, as shown in Figure 5c. Then, FTIR reflection spectra are recorded in each step of the fabrication process, as shown in Figure 5d,e. The resonance wavelengths do not change significantly after oxygen plasma and Ag deposition. The molecular signature of PMMA residues after liftoff can be determined before oxygen plasma. After oxygen plasma, PMMA residues are cleaned and no molecular bands for PMMA are observed. Following 3 nm Ag evaporation, the structures are treated with 1 mM DDT in ethanol solution for monolayer formation. The surfaces are washed with ethanol to remove unattached DDT molecules, and reflection spectra are

dx.doi.org/10.1021/ph500330x | ACS Photonics 2014, 1, 1313−1321

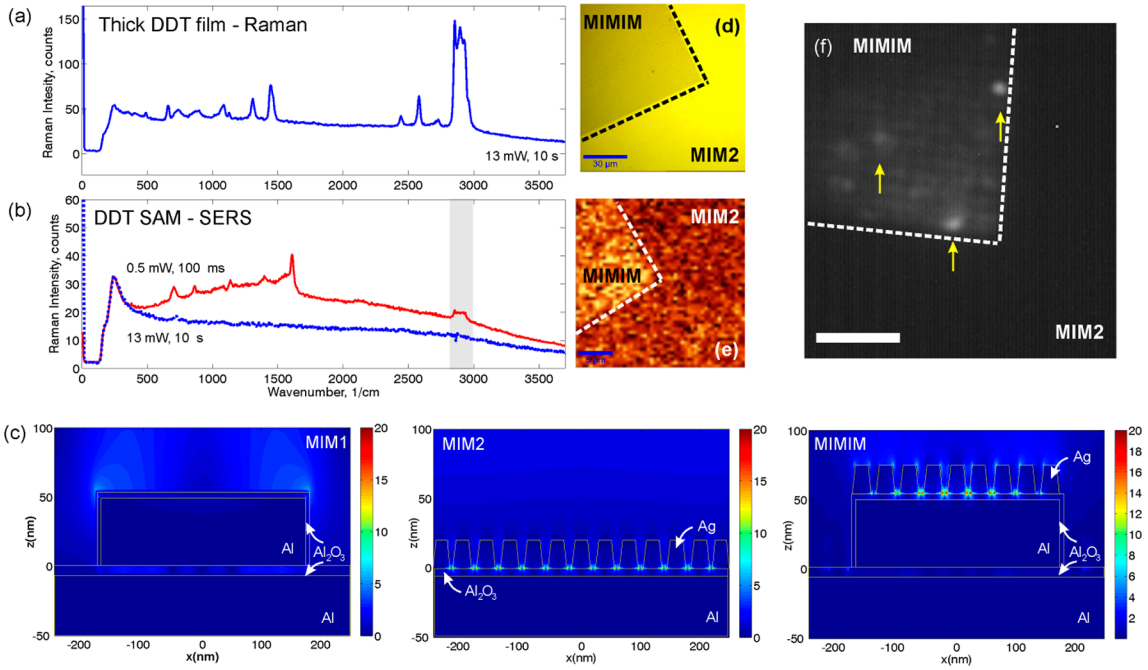

Figure 6. SERS detection of molecular monolayers on hierarchical NO-MIM structures. (a) Raman spectra of a thick DDT solution on 80 nm Al coated silicon. (b) SERS spectra of monolayer DDT on hierarchical NOMIM surfaces and an Al-coated Si substrate. Integration time and laser power are 100 ms and 0.5 mW, respectively, for hierarchical NOMIM surfaces, whereas they are 10 s and 13 mW for Al films on Si. (c) Simulated field profiles for all Al NO-MIM (MIM1), Ag nanoparticle based NO-MIM (MIM2), and hierarchical NO-MIM (MIMIM) structures. (d) Optical micrograph of hierarchical NO-MIM surfaces. (e) SERS mapping of DDT on hierarchical NO-MIM surfaces. Brighter and darker regions emphasize hierarchical NO-MIM and nanoparticle-based NO-MIM structures, respectively. (f) Wide-field CMOS camera image of blink events on NO-MIM structures. Blink events are observed only on hierarchical NO-MIM structures.

recorded. Molecular signatures of DDT molecules can be identified without any postprocessing in the reflection spectra. The first derivative of each reflection spectrum is shown in Figure 5f, which better differentiates the DDT and PMMA signatures. We have also used another method to fabricate PMMA-free NO-MIM surfaces with top Ag layer using focused ion beam (FIB) milling (Figure S10). Since the area that can be fabricated with FIB is smaller compared to e-beam lithography, the resonance contrast in the reflection spectrum from these surfaces is weak (Figure S10d). Other nanofabrication techniques can be used to eliminate the molecular signatures coming from the residues such as nanostencil lithography.[49]

The presence of closely spaced Ag nanoparticles on top of the hierarchical NO-MIM resonators with resonances in the visible and infrared presents an opportunity to perform SERS and SEIRA simultaneously. The Raman spectrum of a thick DDT solution on an Al-covered Si substrate, recorded in 10 s using 13 mW excitation at 532 nm, is shown in Figure 6a. In comparison, SERS data of DDT monolayers formed on hierarchical NO-MIM surfaces are shown in Figure 6b, collected using 0.5 mW excitation and 100 ms integration time. Despite shifts and changes in intensity of several lines, the main features of the spectra are comparable to Raman data shown in Figure 6a. No distinct spectral features of DDT are observed on bare Al films on Si (Figure 6b), since DDT does not stick on Al. It should be noted that, by coinciding the visible resonances of the NO-MIM structures with the resonances of the Ag nanoparticle layer, an enhancement of the field intensities is predicted by computational study of MIMIM structures (Figure 6c, showing $|E|$ distribution). While a small field enhancement is obtained for all Al NO-MIM structures around 532 nm, Ag nanoparticle based NO-MIM structures show improved field enhancement due to better impedance matching of the resonances to free space modes, as well as due to reduced interparticle spacing. In contrast, hierarchical NO-MIM structures show further improvement in field enhancement due to overlapping of the visible resonances of the Al and Ag island layers. The visible resonance is relatively weak and accounts for the diminished reflectance over the hierarchical NO-MIM structures, as shown in Figure 6d. The hierarchical NO-MIM structure however shows improved SERS performance, as shown in the Raman map in Figure 6e (see also Figure S11). When the surface is illuminated by a defocused 532 nm excitation and inspected with a monochrome CMOS camera, blink events,[50] typically associated with single-molecule SERS, are observed on the hierarchical portions of the sample (Figure 6f). Although FDTD calculations suggest an overall SERS enhancement of 1.6×10^5, we attribute the blinking spots to the presence of hot spots with greater field enhancement, due to the random nature of the top Ag nanoisland layer. We have estimated the enhancement factors as 2.2×10^3 for SEIRA and 10^3 for SERS on our multispectral plasmonic structures. These values are comparable to the ones reported in the literature[12,13,S1] and 1 order of magnitude smaller than the reported values in ref 52.

CONCLUSIONS

In conclusion, for the first time we have demonstrated the use of Al and its native Al_2O_3 to fabricate MIM resonators spanning the visible and IR wavelengths. The effect of the NO layer is observed on MIM structures using top nanodisc arrays with resonance in the NIR. Resonance wavelength tuning is demonstrated using a 2D Al bar array as the top layer. The NO layer thickness is extracted by fitting experimental results

dx.doi.org/10.1021/ph500330x | ACS Photonics 2014, 1, 1313−1321

to an analytical model. Simultaneous resonances in the visible and NIR regimes are achieved using a top 1D Al array by exciting multiple plasmon modes in the NO layer. Large-area plasmonic surfaces are fabricated by depositing thin Ag films near the percolation threshold, and the resonance wavelength is tuned by longer exposure of the Al layer to air. Finally, we fabricated hierarchical NO-MIM surfaces using multiple NO layers and percolating Ag films and used these surfaces as SERS and SEIRA substrates for the detection of monolayer DDT. Our results can help to develop more complex Al-based plasmonic structures in the visible and IR regimes for sensing, energy, and metamaterial applications.

METHODS

Design and Fabrication of Plasmonic Devices. Al nanostructured arrays were fabricated by electron-beam lithography on Si substrates coated with 70 nm thick aluminum via thermal evaporation. Before Al we deposited 3 nm germanium on Si as an adhesion layer. A 105 nm thick PMMA resist was spin-coated on top of the aluminum surfaces, then baked at 180 °C for 120 s. An e-beam lithography system consisting of FEI Nova NanoSEM and 600 + Raith ElphyPlus was used to define patterns operating at 30 kV with 26 pA. PMMA resist was developed in a 1:3 solution of methyl isobutyl ketone and isopropyl alcohol for 40 s. The surface was postbaked at 120 °C for 120 s, which was followed by thermal evaporation of 50 nm Al and a final lift-off step in acetone for 4 h.

Optical Characterization. For the IR measurements, Bruker VERTEX 70 Fourier transform infrared spectroscopy with a Hyperion 2000 IR scanning microscope, (15×)NA = 0.4, in reflectance mode was used to get spectral data from plasmonic surfaces. Background spectra were collected from bare aluminum surfaces. Measurements were performed with 2 cm^{-1} resolution and averaged over 64 scans. For the visible measurements, a custom-built reflection setup was used with white light coupled to a 400 μm core multimode fiber. Light output was then collimated using a lens. Collimated light was then sent first through a beam splitter and then focused on the patterned sample using a 20× objective. Reflected light was collected with the same objective and coupled to another 400 μm core multimode fiber with a lens through the beam splitter. The collected light was sent to a UV−vis spectrometer (from Ocean Optics). As the reference, the unpatterned part of the sample coated with Al was used. To characterize the refractive index function of Al and the thickness of native Al_2O_3, we used a spectroscopic ellipsometer in the visible and IR (i.e., JA Woollam Co, V-Vase and IR-Vase).

XPS Measurements. We used a Thermo K-Alpha monochromated high-performance XPS spectrometer for the XPS characterization of the native oxide layer. We measured the binding energy level of Al just after Al deposition (15 min after coating), after 2, 4, 8, and 24 days. To determine the thickness of Al_2O_3, we took measurements from 10 different points on the sample, then averaged the XPS spectra for each data set.

Raman Measurements. SERS measurements were performed using a WITEC Alpha 300S Raman module. A diode-pumped solid-state 532 nm wavelength laser was used for excitation in the Raman measurements. Laser power was measured using a silicon photodiode at the sample plane; power densities were calculated using the spot diameter of the illumination area. For Raman mapping measurements a 100× objective was used. For wide-field SERS measurements, a monochrome CMOS camera (Videology 24C1.3XUSB) was placed on the microscope system.

Self-Assembled Monolayer Preparation. DDT (1 mM) was dissolved in ethanol absolute, and fabricated plasmonic surfaces were immersed in this solution for 16 h. The samples were then washed with ethanol to remove unattached molecules and blow dried with nitrogen in order to form self-assembled monolayers on top of silver nanoislands.

Simulations. Simulations were performed using a commercial FDTD package (Lumerical). For FDTD simulations, symmetric and antisymmetric boundary conditions were used along the x- and y-axes to reduce the computational cost. Perfectly matched layer boundary condition was used in the z-axis. A broadband plane wave (200−1000 nm) was used to calculate the reflection spectrum and magnetic field profiles. The mesh size used in the simulations was 2.5 × 2.5 × 1 nm^3. Dielectric functions used in the simulations are from the program database (CRC data for Al and Palik data for Ag and values adapted from the literature[53] for Al_2O_3). Dielectric functions of Al and Ag were fitted to polynomials with 10^{-5} fit tolerance, 12 coefficients, and 12 imaginary weight using the program's fitting algorithm. The germanium wetting layer was neglected in the simulations. COMSOL was used to confirm FDTD simulations. Floquet periodic boundary conditions were used in x and y directions. Port boundary conditions were used to calculate far-field reflection spectra.

We modeled the MIM structures as planar waveguides. The propagation wavevector β_{SPP} and effective index $n_{eff} = \beta_{SPP}/k_0$ of the fundamental TM mode of a MIM waveguide can be calculated by solving for β_{SPP} in the following equation:[54]

$$k_m\varepsilon_d + k_d\varepsilon_m \tanh\frac{k_d h}{2} = 0$$

where $k_d = (\beta_{SPP}{}^2 - \varepsilon_d k_0{}^2)^{1/2}$, $k_m = (\beta_{SPP}{}^2 - \varepsilon_m k_0{}^2)^{1/2}$, $k_0 = 2\pi/\lambda$ is the propagation wave vector in free space, and h is the dielectric thickness. After numerically solving for complex β_{SPP}, the real part of β_{SPP} was used to calculate the effective index n_{eff}. Assuming a unity magnetic permeability, n_{eff} was used to estimate the impedance of the transmission line using $z_{MIM} = 120\pi/n_{eff}$.

ASSOCIATED CONTENT

Supporting Information

Figures S1, S8, S10, fabrication processes for the NO-MIM surfaces presented in the text; Figure S2, XPS characterization of the native Al_2O_3.; Figure S3, SEM images of asymmetric NO-MIM surfaces; Figure S4, simulation for asymmetric NO-MIM surfaces; Figure S5, SEM image of Ag nanoparticles on silicon and their size distribution; Figure S6, FTIR reflectance spectra for NO-MIM surfaces with Ag top layer; Figure S7, infrared reflection spectra after background subtraction; Figure S9, simulated reflection spectra; Figure S11, Raman spectra for various surfaces. This material is available free of charge via the Internet at http://pubs.acs.org.

AUTHOR INFORMATION

Corresponding Authors

*E-mail (S. Ayas): ayas@bilkent.edu.tr.
*E-mail (A. Dana): aykutlu@unam.bilkent.edu.tr.

Notes

The authors declare no competing financial interest.

■ ACKNOWLEDGMENTS

This work was partially supported by TUBITAK under Grant 111M344 and EU FP7:People-IAPP NanoBacterPhageSERS.

■ REFERENCES

(1) West, P. R.; Ishii, S.; Naik, G. V.; Emani, N. K.; Shalaev, V. M.; Boltasseva, A. Searching for Better Plasmonic Materials. *Laser Photonics Rev.* **2010**, *4*, 795−808.
(2) Jeyaram, Y.; Jha, S. K.; Agio, M.; Löffler, J. F.; Ekinci, Y. Magnetic Metamaterials in the Blue Range Using Aluminum Nanostructures. *Opt. Lett.* **2010**, *35*, 1656.
(3) Taguchi, A.; Saito, Y.; Watanabe, K.; Yijian, S.; Kawata, S. Tailoring Plasmon Resonances in the Deep-Ultraviolet by Size-Tunable Fabrication of Aluminum Nanostructures. *Appl. Phys. Lett.* **2012**, *101*, 081110.
(4) Jha, S. K.; Ahmed, Z.; Agio, M.; Ekinci, Y.; Löffler, J. F. Deep-Ultraviolet Surface-Enhanced Resonance Raman Scattering of Adenine on Aluminum Nanoparticle Arrays. *J. Am. Chem. Soc.* **2012**, *134*, 1966−1969.
(5) Yang, Y.; Callahan, J. M.; Kim, T.-H.; Brown, A. S.; Everitt, H. O. Ultraviolet Nanoplasmonics: A Demonstration of Surface-Enhanced Raman Spectroscopy, Fluorescence, and Photodegradation Using Gallium Nanoparticles. *Nano Lett.* **2013**, *13*, 2837−2841.
(6) Kanehara, M.; Koike, H.; Yoshinaga, T.; Teranishi, T. Indium Tin Oxide Nanoparticles with Compositionally Tunable Surface Plasmon Resonance Frequencies in the near-IR Region. *J. Am. Chem. Soc.* **2009**, *131*, 17736−17737.
(7) Garcia, G.; Buonsanti, R.; Runnerstrom, E. L.; Mendelsberg, R. J.; Llordes, A.; Anders, A.; Richardson, T. J.; Milliron, D. J. Dynamically Modulating the Surface Plasmon Resonance of Doped Semiconductor Nanocrystals. *Nano Lett.* **2011**, *11*, 4415−4420.
(8) Luther, J. M.; Jain, P. K.; Ewers, T.; Alivisatos, A. P. Localized Surface Plasmon Resonances Arising from Free Carriers in Doped Quantum Dots. *Nat. Mater.* **2011**, *10*, 361−366.
(9) Li, S. Q.; Guo, P.; Zhang, L.; Zhou, W.; Odom, T. W.; Seideman, T.; Ketterson, J. B.; Chang, R. P. H. Infrared Plasmonics with Indium-Tin-Oxide Nanorod Arrays. *ACS Nano* **2011**, *5*, 9161−9170.
(10) Naik, G. V.; Liu, J.; Kildishev, A. V.; Shalaev, V. M.; Boltasseva, A. Demonstration of Al:ZnO as a Plasmonic Component for near-Infrared Metamaterials. *Proc. Natl. Acad. Sci. U.S.A.* **2012**, *109*, 8834−8838.
(11) Brar, V. W.; Jang, M. S.; Sherrott, M.; Lopez, J. J.; Atwater, H. A. Highly Confined Tunable Mid-Infrared Plasmonics in Graphene Nanoresonators. *Nano Lett.* **2013**, *13*, 2541−2547.
(12) Abb, M.; Wang, Y.; Papasimakis, N.; de Groot, C. H.; Muskens, O. L. Surface-Enhanced Infrared Spectroscopy Using Metal Oxide Plasmonic Antenna Arrays. *Nano Lett.* **2014**, *14*, 346−352.
(13) Yu, L.; Rosenberg, A.; Wasserman, D. All-Semiconductor Plasmonic Nanoantennas for Infrared Sensing. *Nano Lett.* **2013**, *13*, 4569−4574.
(14) Lezec, H. J.; Dionne, J. a; Atwater, H. a. Negative Refraction at Visible Frequencies. *Science* **2007**, *316*, 430−432.
(15) Xu, T.; Agrawal, A.; Abashin, M.; Chau, K. J.; Lezec, H. J. All-Angle Negative Refraction and Active Flat Lensing of Ultraviolet Light. *Nature* **2013**, *497*, 470−474.
(16) Zentgraf, T.; Liu, Y.; Mikkelsen, M. H.; Valentine, J.; Zhang, X. Plasmonic Luneburg and Eaton Lenses. *Nat. Nanotechnol.* **2011**, *6*, 151−155.
(17) Homola, J.; Yee, S. S.; Gauglitz, G. Surface Plasmon Resonance Sensors: Review. *Sens. Actuators, B* **1999**, *54*, 3−15.
(18) McFarland, A. D.; Van Duyne, R. P. Single Silver Nanoparticles as Real-Time Optical Sensors with Zeptomole Sensitivity. *Nano Lett.* **2003**, *3*, 1057−1062.
(19) Shafer-Peltier, K. E.; Haynes, C. L.; Glucksberg, M. R.; Van Duyne, R. P. Toward a Glucose Biosensor Based on Surface-Enhanced Raman Scattering. *J. Am. Chem. Soc.* **2003**, *125*, 588−593.
(20) Nie, S.; Emory, S. R. Probing Single Molecules and Single Nanoparticles by Surface-Enhanced Raman Scattering. *Science* **1997**, *275*, 1102−1106.
(21) Brown, L. V.; Zhao, K.; King, N.; Sobhani, H.; Nordlander, P.; Halas, N. J. Surface-Enhanced Infrared Absorption Using Individual Cross Antennas Tailored to Chemical Moieties. *J. Am. Chem. Soc.* **2013**, *135*, 3688−3695.
(22) Adato, R.; Yanik, A. a; Amsden, J. J.; Kaplan, D. L.; Omenetto, F. G.; Hong, M. K.; Erramilli, S.; Altug, H. Ultra-Sensitive Vibrational Spectroscopy of Protein Monolayers with Plasmonic Nanoantenna Arrays. *Proc. Natl. Acad. Sci. U.S.A.* **2009**, *106*, 19227−19232.
(23) Atwater, H. a; Polman, A. Plasmonics for Improved Photovoltaic Devices. *Nat. Mater.* **2010**, *9*, 205−213.
(24) Knight, M. W.; Sobhani, H.; Nordlander, P.; Halas, N. J. Photodetection with Active Optical Antennas. *Science* **2011**, *332*, 702−704.
(25) Naik, G. V.; Shalaev, V. M.; Boltasseva, A. Alternative Plasmonic Materials: Beyond Gold and Silver. *Adv. Mater.* **2013**, *25*, 3264−3294.
(26) Reed, J. C.; Zhu, H.; Zhu, A. Y.; Li, C.; Cubukcu, E. Graphene-Enabled Silver Nanoantenna Sensors. *Nano Lett.* **2012**, *12*, 4090−4094.
(27) Chowdhury, M. H.; Ray, K.; Gray, S. K.; Pond, J.; Lakowicz, J. R. Aluminum Nanoparticles as Substrates for Metal-Enhanced Fluorescence in the Ultraviolet for the Label-Free Detection of Biomolecules. *Anal. Chem.* **2009**, *81*, 1397−1403.
(28) Chan, G. H.; Zhao, J.; Schatz, G. C.; Van Duyne, R. P. Localized Surface Plasmon Resonance Spectroscopy of Triangular Aluminum Nanoparticles. *J. Phys. Chem. C* **2008**, *112*, 13958−13963.
(29) Sigle, D. O.; Perkins, E.; Baumberg, J. J.; Mahajan, S. Reproducible Deep-UV SERRS on Aluminum Nanovoids. *J. Phys. Chem. Lett.* **2013**, *4*, 1449−1452.
(30) Maidecchi, G.; Gonella, G.; Proietti Zaccaria, R.; Moroni, R.; Anghinolfi, L.; Giglia, A.; Nannarone, S.; Mattera, L.; Dai, H.-L.; Canepa, M.; et al. Deep Ultraviolet Plasmon Resonance in Aluminum Nanoparticle Arrays. *ACS Nano* **2013**, *7*, 5834−5841.
(31) Knight, M. W.; Liu, L.; Wang, Y.; Brown, L.; Mukherjee, S.; King, N. S.; Everitt, H. O.; Nordlander, P.; Halas, N. J. Aluminum Plasmonic Nanoantennas. *Nano Lett.* **2012**, *12*, 6000−6004.
(32) Ordal, M. a; Long, L. L.; Bell, R. J.; Bell, S. E.; Bell, R. R.; Alexander, R. W.; Ward, C. a. Optical Properties of the Metals Al, Co, Cu, Au, Fe, Pb, Ni, Pd, Pt, Ag, Ti, and W in the Infrared and Far Infrared. *Appl. Opt.* **1983**, *22*, 1099−20.
(33) Martin, J.; Proust, J.; Gérard, D.; Plain, J. Localized Surface Plasmon Resonances in the Ultraviolet from Large Scale Nano-structured Aluminum Films. *Opt. Mater. Express* **2013**, *3*, 954.
(34) Maidecchi, G.; Gonella, G.; Proietti Zaccaria, R.; Moroni, R.; Anghinolfi, L.; Giglia, A.; Nannarone, S.; Mattera, L.; Dai, H.-L.; Canepa, M.; et al. Deep Ultraviolet Plasmon Resonance in Aluminum Nanoparticle Arrays. *ACS Nano* **2013**, *7*, 5834−5841.
(35) Zoric, I.; Zach, M.; Kasemo, B.; Langhammer, C. Gold, Platinum, and Aluminum Nanodisk Plasmons: Material Independence, Subradiance, and Damping Mechanisms. *ACS Nano* **2011**, *5*, 2535−2546.
(36) Tan, S. J.; Zhang, L.; Zhu, D.; Goh, X. M.; Wang, Y. M.; Kumar, K.; Qiu, C.-W.; Yang, J. K. W. Plasmonic Color Palettes for Photorealistic Printing with Aluminum Nanostructures. *Nano Lett.* **2014**, *14*, 4023−4029.
(37) Ekinci, Y.; Solak, H. H.; Löffler, J. F. Plasmon Resonances of Aluminum Nanoparticles and Nanorods. *J. Appl. Phys.* **2008**, *104*, 083107.
(38) Knight, M. W.; King, N. S.; Liu, L.; Everitt, H. O.; Nordlander, P.; Halas, N. J. Aluminum for Plasmonics. *ACS Nano* **2014**, *8*, 834−840.
(39) Mazzotta, F.; Wang, G.; Hägglund, C.; Höök, F.; Jonsson, M. P. Nanoplasmonic Biosensing with on-Chip Electrical Detection. *Biosens. Bioelectron.* **2010**, *26*, 1131−1136.
(40) Homola, J. Present and Future of Surface Plasmon Resonance Biosensors. *Anal. Bioanal. Chem.* **2003**, *377*, 528−539.

(41) Ozbay, E. Plasmonics: Merging Photonics and Electronics at Nanoscale Dimensions. *Science* **2006**, *311*, 189−193.
(42) Oulton, R. F.; Sorger, V. J.; Genov, D. a.; Pile, D. F. P.; Zhang, X. A Hybrid Plasmonic Waveguide for Subwavelength Confinement and Long-Range Propagation. *Nat. Photonics* **2008**, *2*, 496−500.
(43) Hryciw, A.; Jun, Y. C.; Brongersma, M. L. Plasmonics: Electrifying Plasmonics on Silicon. *Nat. Mater.* **2010**, *9*, 3−4.
(44) Dionne, J. A.; Sweatlock, L. a.; Sheldon, M. T.; Alivisatos, A. P.; Atwater, H. A. Silicon-Based Plasmonics for On-Chip Photonics. *IEEE J. Sel. Top. Quantum Electron.* **2010**, *16*, 295−306.
(45) Langhammer, C.; Schwind, M.; Kasemo, B.; Zoric, I. Localized Surface Plasmon Resonances in Aluminum Nanodisks. *Nano Lett.* **2008**, *8*, 1461−1471.
(46) Knight, M. W.; King, N. S.; Liu, L.; Everitt, H. O.; Nordlander, P.; Halas, N. J. Aluminum for Plasmonics. *ACS Nano* **2014**, *8*, 834−840.
(47) Laibinis, P. E.; Whitesides, G. M.; Allara, D. L.; Tao, Y.-T.; Parikh, A. N.; Nuzzo, R. G. Comparison of the Structures and Wetting Properties of Self-Assembled Monolayers of *n*-Alkanethiols on the Coinage Metal Surfaces, Cu, Ag, Au. *J. Am. Chem. Soc.* **1991**, *113*, 7152−7167.
(48) Neubrech, F.; Pucci, A.; Cornelius, T.; Karim, S.; García-Etxarri, A.; Aizpurua, J. Resonant Plasmonic and Vibrational Coupling in a Tailored Nanoantenna for Infrared Detection. *Phys. Rev. Lett.* **2008**, *101*, 157403.
(49) Aksu, S.; Huang, M.; Artar, A.; Yanik, A. A.; Selvarasah, S.; Dokmeci, M. R.; Altug, H. Flexible Plasmonics on Unconventional and Nonplanar Substrates. *Adv. Mater.* **2011**, *23*, 4422−4430.
(50) Ayas, S.; Cupallari, A.; Ekiz, O. O.; Kaya, Y.; Dana, A. Counting Molecules with a Mobile Phone Camera Using Plasmonic Enhancement. *ACS Photonics* **2014**, *1*, 17−26.
(51) Andrea, C. D.; Toma, A.; Huck, C.; Neubrech, F.; Messina, E.; Fabrizio, E. Di; Lamy, M.; Chapelle, D. La; Gucciardi, P. G.; Fazio, B.; et al. Optical Nanoantennas for Multiband Surface-Enhanced Infrared and Raman Spectroscopy. *ACS Nano* **2013**, *7*, 3522−3531.
(52) Aouani, H.; Rahmani, M.; Šípová, H.; Torres, V.; Hegnerová, K.; Beruete, M.; Homola, J.; Hong, M.; Navarro-Cía, M.; Maier, S. A. Plasmonic Nanoantennas for Multispectral Surface-Enhanced Spectroscopies. *J. Phys. Chem. C* **2013**, *117*, 18620−18626.
(53) Kischkat, J.; Peters, S.; Gruska, B.; Semtsiv, M.; Chashnikova, M.; Klinkmüller, M.; Fedosenko, O.; Machulik, S.; Aleksandrova, A.; Monastyrskyi, G.; et al. Mid-Infrared Optical Properties of Thin Films of Aluminum Oxide, Titanium Dioxide, Silicon Dioxide, Aluminum Nitride, and Silicon Nitride. *Appl. Opt.* **2012**, *51*, 6789−6798.
(54) Kaminow, I. P.; Mammel, W. L.; Weber, H. P. Metal-Clad Optical Waveguides: Analytical and Experimental Study. *Appl. Opt.* **1974**, *13*, 396.